

SHIELDING AND RADIATION

**H. DeStaebler, T. M. Jenkins, Coeditor,
and W. R. Nelson, Coeditor**

The purpose of this chapter is to present a simplified logic useful in understanding the shielding around a high-energy electron accelerator. This should be useful in cases where a shield is to be designed for radiation worker tolerance and in cases where a shield already exists and some knowledge of the radiation penetrating that shield is required.

Certain basic assumptions are made which should be discussed here. First, the energy spectrum of radiation penetrating a shield is assumed to be known, or to be approximated in such a way that a flux-to-dose conversion may be made. Second, the problem of distant boundaries is assumed to be secondary to that of the radiation worker in close proximity to the shield, so that to a first-order approximation, skyshine, etc., may be ignored.

Shielding calculations are done in distinct steps:

1. First, one must determine the radiation tolerances. At SLAC this value is 0.75 mrem/hour (steady occupancy). To be conservative, one should design shielding to produce about one-tenth of the steady occupancy value.
2. The amount of average electron beam power stopped within the shield must be estimated.
3. One must derive some information on the development of the electromagnetic cascade.
4. One must determine the production of penetrating particles by the cascade.
5. Finally, the attenuation of these penetrating particles in the shield has to be calculated.

This chapter is concerned with items (3), (4), and (5) above. First, the electromagnetic cascade and the production of penetrating particles by that

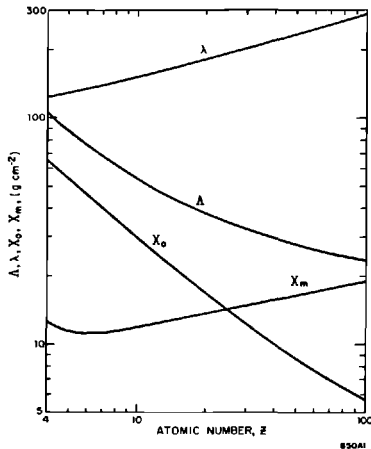
cascade will be examined. Then, the shielding problem will be approached from the standpoint of having to shield the least penetrating component (photon radiation) first, go on to the next more penetrating component (neutrons), and finally, take up the problem of shielding muons which are very weakly interacting. A brief discussion concerning radiation streaming up penetrations will follow. And in conclusion, an outline for making practical (order-of-magnitude) calculations will be presented.

26-1 Electromagnetic cascade (HDeS, WRN)

When a high-energy electron or photon enters an absorber, an electromagnetic cascade shower is produced. The basic interactions of the electrons and photons are well established, but analytical solutions of the diffusion equations are prohibitively difficult to obtain. Analytic shower theory^{1,2} accounts for the main features of the longitudinal or one-dimensional development of the cascade. Usually for shielding calculations the behavior at great depths is needed where approximation in the theory may have important consequences. Few experiments go deeper than 15 or 20 radiation lengths³⁻⁵ (denoted by X_0), but these experiments and simple theory agree that the shower decreases exponentially with an absorption mean free path of several radiation lengths. This agreement may be accidental, however, because the most penetrating component, which one would expect to control the shower at great depths, consists of photons with energies near the minimum in the interaction cross section* (hence, with the greatest mean free path, denoted by $\Lambda \equiv 1/\mu_{\min}$,

*These are the good geometry values which are given many places, for example, Reference 6.

Figure 26-1 The variation of Λ , λ , X_0 , and X_m with atomic number, Z .



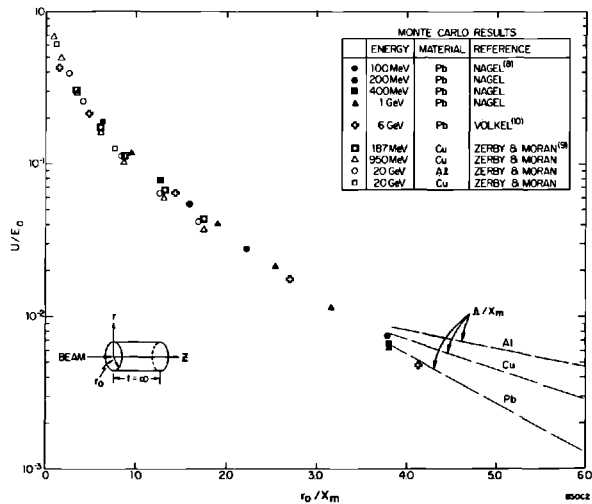
where μ_{\min} is the narrow beam, minimum absorption coefficient). In most analytic shower theories, there are approximations that eliminate this minimum in the photon cross section. Figure 26-1 shows that Λ varies from about $2X_0$ at low Z to about $4X_0$ at high Z . Scattering, which decreases the effective absorption length in a real three-dimensional shower, is more important at high Z because the average electron energy is lower, and an absorption mean free path around $3X_0$ is reasonable for all Z .

The radial or transverse spread requires three-dimensional shower theory⁷ which is too complicated to be done very accurately analytically and application is limited to high-energy cosmic-ray phenomena. The most useful calculations are the Monte Carlo studies,⁸⁻¹⁰ which take into account the important cross-section data and which do not introduce as many oversimplifications. Experiments are complicated by the requirements of large dynamic range in the detector and small sizes for the incident beam and the detector.^{3,11,12} For shielding applications a useful way to summarize the Monte Carlo results is to consider the energy absorbed per unit volume, dw/dv . Define the fraction of the total energy E_0 absorbed beyond radius r_0 by

$$\frac{U(r_0)}{E_0} = \frac{\int_0^\infty \int_{r_0}^\infty \frac{dw}{dv} 2\pi r dr dz}{\int_0^\infty \int_0^\infty \frac{dw}{dv} 2\pi r dr dz} \tag{26-1}$$

Figure 26-2 gives U/E_0 versus r_0 in Moliere units. A Moliere unit, X_m , is the characteristic measure for radial distributions in analytic shower theory¹³ and

Figure 26-2 The fraction of the total shower energy that is absorbed beyond a cylindrical radius, r_0 , as a function of r_0/X_m .



is equal to $X_0 E_s/\epsilon_0$, where ϵ_0 is the critical energy of the material and $E_s = 21.2$ MeV. The values of X_0 and X_m used¹⁴ are given in Fig. 26-1. The significance of Fig. 26-2, for shielding purposes, is that a universal curve is formed. The result is independent of incident energy and target material. The behavior of U/E_0 at large r_0 is of interest, but unfortunately the Monte Carlo calculations do not extend far enough out. Again, one would expect the most penetrating component (namely, those photons having a mean free path, Λ) to control the shower at large radial depths. Shown on Fig. 26-2 are the slopes corresponding to Λ (in Moliere units) for aluminum, copper, and lead.

26-2 Production and attenuation of photon radiation from thick targets (TMJ, WRN)

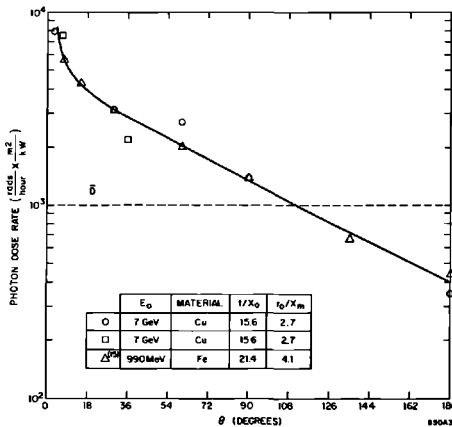
It is of practical interest to determine the angular distribution of photon radiation for high-energy electron beams striking thick targets. Consider a cylindrical target having a length of $\approx 15X_0$ and a radius of $\approx 3X_m$. One would expect, according to Fig. 26-2, that about 1% of the total energy would escape radially. Assuming that this energy is radiated isotropically into 4π steradians, one can make an order of magnitude calculation of the dose rate at 1 meter for 1 kW of incident beam power.

$$\bar{D} = \frac{10^{-2} \times 10^3 \text{ W} \times 10^7 \text{ ergs-sec}^{-1} \text{ W}^{-1}}{4\pi(10^2 \text{ cm})^2 30 \text{ g-cm}^{-2}} \times \frac{1 \text{ rad}}{10^2 \text{ ergs-g}^{-1}} \times \frac{3600 \text{ sec}}{\text{hour}}$$

$$\sim 10^3 \text{ rad/hour}$$

where 30 g-cm^{-2} is an average value for Λ .

Figure 26-3 The photon dose rate from a typical beam absorber as a function of the angle from the beam direction, normalized to 1 kW of beam power and to a source-to-detector distance of 1 meter.



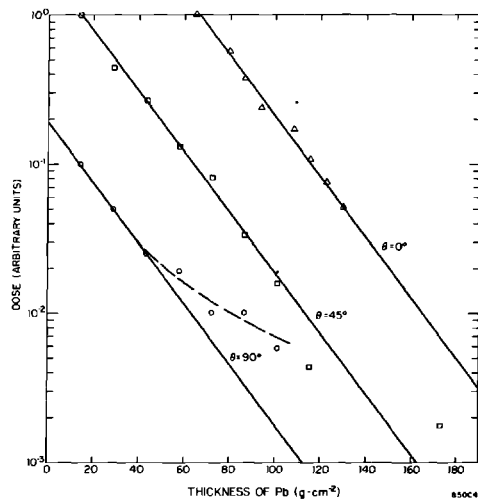
This order of magnitude is verified in Fig. 26-3 where several measurements are plotted versus the angle from the beam direction, the cylinder considered a point source. Measurements at 0° have been made but are not shown in Fig. 26-3 because they are too dependent on incident beam energy, target thickness, and detector size (the dose rate falls off rather sharply with angle, as seen in Fig. 26-3).

For $E_0 = 990$ MeV, $t = 21.4X_0$, and using a Zeus ion chamber, Neet¹⁵ has measured 1.1×10^4 rads/hour at 0° and for 1 kW at 1 meter. On the other hand, we have measured 1.2×10^5 rads/hour for $E_0 = 12$ GeV, $t = 16X_0$, and using a small ($\frac{1}{8}$ in.) capsule of LiF.

Gamma-ray absorption measurements have been made at 0° , 45° , and 90° by placing capsules of LiF powder between lead plates and by exposing the arrangement to the radiation coming from an iron cylinder ($t = 16X_0$, $r_0 = 3.6X_m$) bombarded by a 12-GeV electron beam. The LiF responds to ionizing radiation and its use for this purpose is described elsewhere.¹⁶ Figure 26-4 shows the absorption for these three angles as a function of lead thickness. The 90° measurement was complicated by the presence of the 20-GeV spectrometer, the backscattering from which might account for the departure from a straight line, as indicated in Fig. 26-4 by the broken line.

One would expect, according to the simple theory above, that the most probable gamma-ray energy would be ≈ 8 MeV, corresponding to the

Figure 26-4 Absorption measurements in lead for γ radiation coming from an iron target that is bombarded with a 12-GeV electron beam, for various angles from the beam direction ($t = 16X_0$, $r_0 = 3.6X_m$).



minimum in the narrow-beam absorption curve for iron. The absorption coefficient, μ , in lead at 8 MeV is $0.047 \text{ cm}^2/\text{g}$, which is the slope of the straight lines in Fig. 26-4.

One can apply the above curves and theory to a typical shielding situation. Consider a copper target ($t = 15.6X_0$, $r_0 = 2.7X_m$) located in end station A as shown in Fig. 26-5. The beam energy is 7 GeV and the power is 1 kW. Using Fig. 26-3 along with the narrow-beam absorption coefficient in concrete at 9 MeV, one obtains the dose rates around the end station given in Table 26-1. Also given are the actual gamma-ray measurements taken under the above conditions.

At positions B and G the calculation agrees within the measuremental errors. At positions C and F the measurements are higher than the calculations; however, this could very well be due to scattering around the entrance maze. (Using the unattenuated calculated dose rates at the entrance modules and allowing 5% of the photon radiation for each 90° bend, one obtains about the dose rate actually measured.) At positions D and E the calculation fails—although account should probably be taken of the much higher levels at close to zero angle that have scattered in the air path between the target

Figure 26-5 Plan view of end station A, indicating the positions where photon and neutron measurements were made.

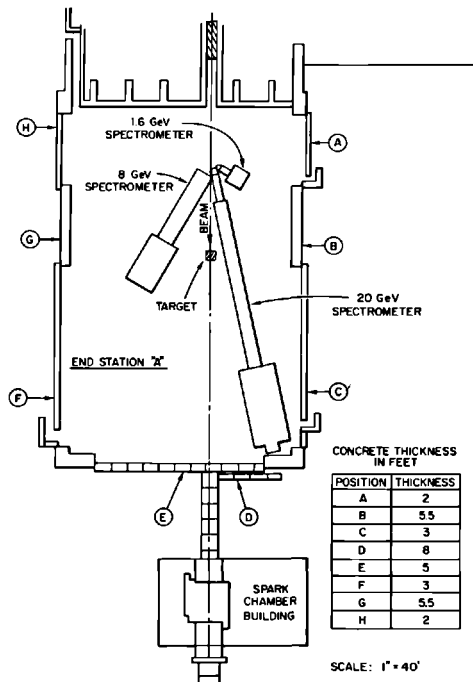


Table 26-1 Comparison of calculated and measured photon dose rates around end station A

<i>Position^a</i>	<i>Calculated dose rate (mR/hour)</i>	<i>Measured dose rate (mR/hour)</i>
A	12	5–6
B	0.5	0.5–2.5
C	0.2	4–5
D	0.007	2.5–3.8
E	1.0	18–38
F	0.4	7.5
G	0.7	0–2.5
H	7.5	2.5–4

^a See Fig. 26-5; $E_0 = 7$ GeV; beam power = 1 kW.

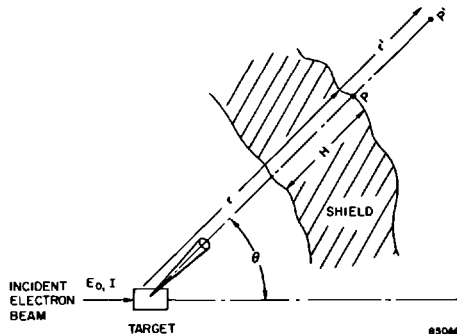
and the end station wall. Also, the method of calculation seems to overestimate the dose rate at position A—particularly if one again accounts for the radiation that comes through the entrance maze. One might expect that the average gamma-ray energy in the backward direction would be considerably lower than 8–9 MeV, and hence, a much larger absorption coefficient should be used. It appears, however, that one can estimate the photon dose rate within a factor of 2 or 3, except in the forward ($\theta \lesssim 10^\circ$) direction.

26-3 Neutron production and attenuation (HDeS, TMJ)

Outline of general calculation

The procedure outlined here for calculating the photonuclear shielding is fairly simple. It is basically the same as that first used for reactor shielding, and in many details it is a direct application of the scheme developed by

Figure 26-6 Schematic of a typical shielding geometry.



Moyer and co-workers and applied to the 184-in. cyclotron and to the bevatron.^{17,18}

Figure 26-6 shows the general layout and defines some symbols. Assuming a point source, the radiation level at a point P on the outside surface of the shield is

$$D_P = \frac{1}{r^2} \int F(T)B(T) \exp\left[\frac{-H(\theta)}{\lambda(T)}\right] \frac{d^2n(T, \theta)}{dT d\Omega} dT \quad (26-2)$$

where

T = the neutron kinetic energy

r = the distance from target to P

F = the biological conversion factor (rem/neutrons-cm⁻²)

H = the shield thickness

λ = the effective removal mean free path

B = the buildup factor so that $Be^{-H/\lambda}$ represents the tail of the nuclear cascade

$\frac{d^2n}{dT d\Omega}$ = the yield of neutrons into (T, dT) and $(\theta, d\Omega)$ arising from the absorption of an electron beam with current I and energy E_0

At low energies $B \approx 1$ and F is well established¹⁹; at high energies, $BF \equiv G$ may be taken from the work of Neary and Mulvey.²⁰

Equation (26-2) may be written

$$D_P = \frac{1}{r^2} \sum G_i \exp\left(\frac{-H}{\lambda_i}\right) \frac{dn_i}{d\Omega} \quad (26-3)$$

where the subscript i denotes a range of neutron energies for which G and λ are fairly constant, and

$$\frac{dn_i}{d\Omega} = \int_{T_i}^{T_{i+1}} \frac{d^2n}{dT d\Omega} dT \quad (26-4)$$

Moyer approximated the sum in Eq. (26-3) by a single term (since below 200 MeV, λ decreases rapidly as T decreases^{18,21}) with $\lambda = 158$ g/cm², which is typical of the effective removal mean free path in concrete for neutrons with energies above several hundred million electron volts (see Fig. 26-1), and with

$$\frac{dn(\varepsilon, \theta)}{d\Omega} = \int_{\varepsilon}^{T_{\max}(\theta, E_0)} \frac{d^2n}{dT d\Omega} dT \quad (26-5)$$

with $\varepsilon = 150$ MeV.

The distribution in angle and energy of photoneutrons has not been measured extensively above roughly 100 MeV. In an approximate calculation,

fictitious two-body reactions replace the actual complicated reactions.²² Then

$$\frac{d^2n}{dT d\Omega} = I \int \frac{N_0}{A} \frac{d\sigma(k, \theta^*)}{d\Omega^*} \frac{\partial(k, \theta^*)}{\partial(T, \theta)} \frac{dl}{dk} dk \quad (26-6)$$

where

I = the incident electron current

N_0, A = Avogadro's number, atomic weight

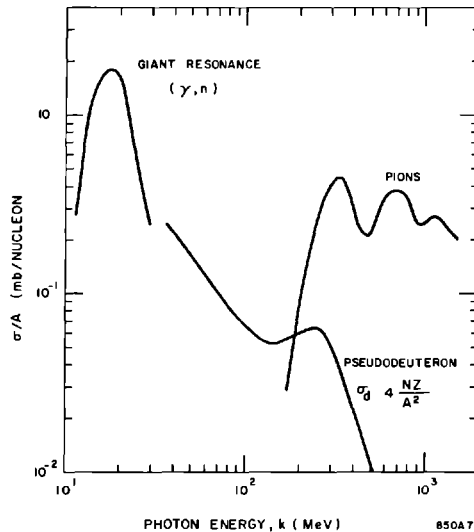
$\frac{d\sigma}{d\Omega^*} = \sigma_{\text{total}}/4\pi$ if isotropy in the center of mass is assumed

$\frac{\partial(k, \theta^*)}{\partial(T, \theta)}$ = the Jacobian from variable transformation

$\frac{dl}{dk}$ = the differential photon track length, $0.57 E_0 X_0/k^2$

The total cross sections are shown in Fig. 26-7. For thin shields the giant resonance reactions dominate; these have been studied extensively.²³⁻²⁵ For thick shields, the pion reactions²⁶ are most important. The pseudodeuteron reaction²³ always contributes but never dominates. The $1/k^2$ variation of the photon track length makes the neutron yields insensitive to the behavior of the cross section at higher energies. Preliminary measurements²⁷ up to 5 BeV are consistent with σ_{total} roughly constant of the order of 100 mb/nucleon, and there is some evidence that σ_{total} decreases at very high energies.²⁸

Figure 26-7 Total photonuclear cross section divided by the atomic weight (millibarns/nucleon) as a function of the photon energy.



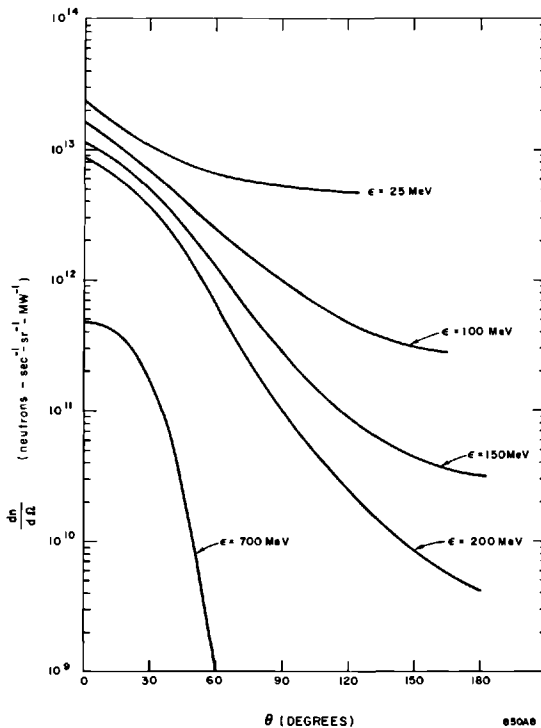
The two-body approach of Eq. (26-6) gives reasonable agreement with the measured spectra of photoprotons with $50^\circ < \theta < 94^\circ$ from 950-MeV bremsstrahlung on copper.²² Figure 26-8 shows $dn/d\Omega$, essentially Eq. (26-5) from Eq. (26-6), for electrons on copper for $\epsilon = 100, 150,$ and 200 MeV. Note that for electrons, $dn/d\Omega$, and hence D_p is proportional to IE_0 (the incident beam power) and to X_0 (via dl/dk). The values for $\epsilon = 25$ MeV and $\epsilon = 700$ MeV were extrapolated from the 100-, 150-, and 200-MeV calculations and are included in Fig. 26-8. Figure 26-9 shows $r^2 D_p$ derived from Fig. 26-8 and Eq. (26-3) with five energy groups and Moyer's curve for $\lambda(T)$.

Some comments on this whole procedure may be appropriate.

1. This approach is sometimes called semiempirical because λ is determined from experiment. Although $dn/d\Omega$ and G are based upon reasonable, yet approximate, calculations, various measurements indicate that there are no gross errors.

2. In the model implied by Eq. (26-2) and Fig. 26-6, there is no spreading of the nuclear cascade in the shield. All of the spreading arises from the

Figure 26-8 High-energy neutron production by electrons on copper as a function of angle. The curves indicate the number of neutrons with energies greater than ϵ .



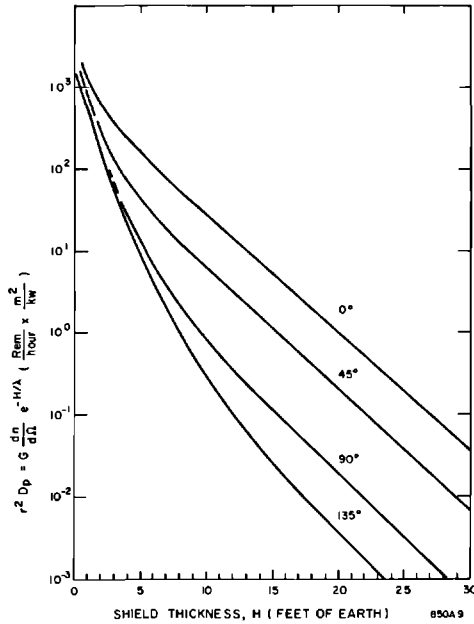


Figure 26-9 Normalized neutron radiation level ($r^2 D_p$, in Eq. (26-3)) for $\theta = 0^\circ$, 45° , 90° , and 135° as a function of the shield thickness, H , in feet of earth-equivalent ($\rho = 1.70 \text{ g-cm}^{-3}$).

angular distributions of the neutrons from the source. These approximations are better the more uniform the shield thickness and the greater the separation between target and shield.

3. Since the cascade is taken to be one-dimensional ("straight-ahead" approximation), λ should be derived from a bad geometry experiment.

4. Empirically, λ scales with the inelastic σ at high energies and with the total σ at low energies.¹⁸ These cross sections vary approximately²⁹ as $A^{3/4}$, so for different materials λ is proportional to $A^{1/4}$ (in which case the effective A of concrete is 23.3) and this is the variation of λ shown in Fig. 26-1.

5. Most of the radiation field at the outer surface of the shield consists of low-energy particles, the secondaries in equilibrium with the penetrating high-energy particles. These secondaries have a broad angular distribution so that simply replacing r by $r + r'$ in Eq. (26-2) may not give a good estimate of D_p , the radiation level at P' (see Fig. 26-6). A better procedure is to treat the surface of the shield as a new source by integrating D_p over the surface of the shield and letting it reradiate according to some new angular distribution, for example, isotropic into 1 or 2π , or cosine.

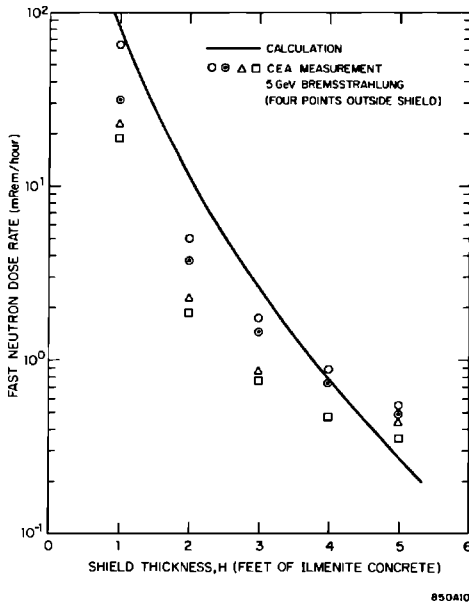


Figure 26-10 Comparison of a Cambridge electron accelerator shielding experiment with calculation. The fast neutron dose rate is plotted versus the shield thickness (Ilmenite concrete, $\rho = 4.0 \text{ g-cm}^{-3}$). Photon beam intensity $= 2.0 \times 10^{10}$ eq. quanta/sec; see Reference 30.

As an example of the application of all this, Fig. 26-10 compares measurements made at the Cambridge electron accelerator³⁰ with the present method of calculation. The points are the levels actually measured with a Bonner sphere dosimeter (uncorrected for background) at four points outside the shield. The calculation is based on (1) a rough interpolation between 45° and 90° curves on Fig. 26-9, (2) a factor of 0.5 accounting for the fact that the dosimeter only measures part of the level, and (3) the level at the surface of the shield being integrated over (multiplied by) 2π steradians and reradiated isotropically into one-quarter of a sphere with a radius of 10 ft. Considering the crudeness of this estimate, the agreement is amazingly close.

Measurements of photoneutrons

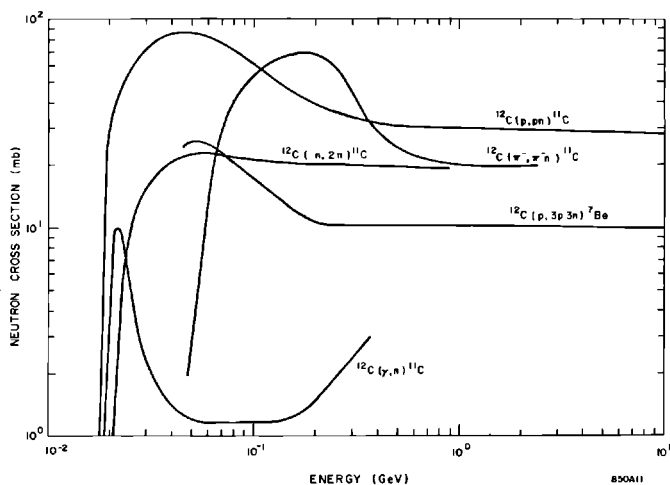
For shielding against radiation produced in a high-energy accelerator, one would like to know the energy-flux distribution of neutrons incident upon a shield. Except in the forward direction where muons become significant, neutrons with energies between 200 and 500 MeV dominate the shielding

calculations in a high-energy accelerator. Neutrons with higher energies are very rare because there are few high-energy photons, and neutrons with lower energies have short attenuation lengths and are easily absorbed. For areas of thin shielding, such as the end stations where walls may be only a few feet thick, one needs to know the neutron production fairly well in order to make an accurate estimate of radiation penetrating the shield. For these reasons, the accuracy of neutron production calculations, and particularly Fig. 26-8, were checked in a series of experiments using a high-energy electron beam. The yield of neutrons was measured in the 0° direction at an electron energy $E_0 = 10$ GeV with $\varepsilon = 700$ MeV and with $\varepsilon = 25$ MeV. The yield for $E_0 = 7$ GeV with $\varepsilon = 25$ MeV was also measured at 0° , 30° , 60° , and 90° .

Measurements of neutrons with $E_n > 25$ MeV were made using the $^{12}\text{C}(n, 2n)^{11}\text{C}$ reaction which has a threshold of ≈ 20 MeV. Normally, this reaction has been utilized only outside of shielding where competing reactions from high-energy photons and charged particles are not probable. However, inside the shielding, photons, pions, and protons will tend to mask the $(n, 2n)$ reaction to a degree determined by particle production cross sections and reaction cross sections leading to ^{11}C . Figure 26-11 shows the cross sections for reactions in carbon leading to ^{11}C as given in the literature.³¹

The carbon is in the form of a plastic scintillator 5 in. in diameter and 5 in. high, coated with white paint. The scintillators were first irradiated and then removed for counting on a 5-in. photomultiplier tube encased in a lead-lined iron housing. Sensitivity of the system is such that a unit flux density of neutrons with $E_n > 20$ MeV will give 105 counts/min. Normal background is about 800 counts/min.

Figure 26-11 Reaction cross sections in carbon leading to ^{11}C (taken from Reference 31). Also shown is the reaction leading to ^7Be ($T_{1/2} = 53$ days).



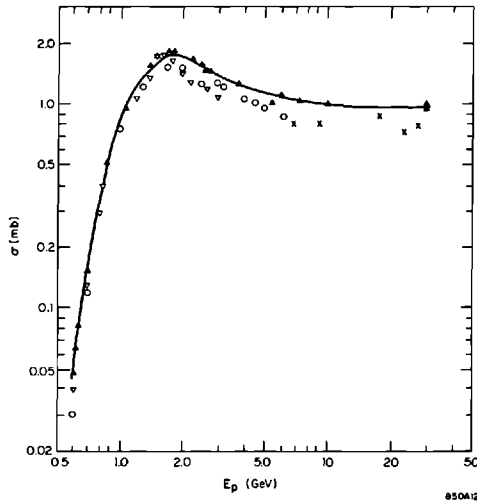


Figure 26-12 Cross section for the reaction $^{197}\text{Au} + p \rightarrow ^{149}\text{Tb}$ (taken from Reference 33). The $^{197}\text{Au} + n \rightarrow ^{149}\text{Tb}$ cross section is assumed to be the same. The threshold, shape, and magnitude for the reaction in mercury should be similar to gold (Reference 32).

Neutrons with energies greater than 700 MeV were measured with mercury detectors. The high-energy spallation reaction in Hg has been reported by McCaslin *et al.*,³² with a threshold for producing ^{149}Tb between 300 and 700 MeV. The threshold and cross sections should be essentially the same as that for the spallation of Au leading to ^{149}Tb as reported by Franz and Friedlander³³ (see Fig. 26-12), who give a threshold for the $^{197}\text{Au} (p, \text{spallation}) ^{149}\text{Tb}$ reaction between 500 and 600 MeV with a cross section of about 1 mb. It is assumed that the reaction cross section for ^{149}Tb production from neutrons is similar to that from protons. Inside shielding, this detector measures the reaction from pions, protons, neutrons, and perhaps high-energy photons. However, in SLAC measurements, a thick copper target ($\approx 16X_0$) was used. There should not be many surviving photons with energies great enough to produce this reaction. Thus, this detector should give numbers closer to calculation than the carbon detector where there may be a significant number of photons with $E_\gamma \gtrsim 20$ MeV, especially in the forward direction. The mercury was irradiated in polyethylene jars and then removed to a laboratory* for analysis. There they were placed in a centrifuge rotating at 1700 *g* for 1 hour with a cellulose acetate pressure-sensitive tape on top. The tape

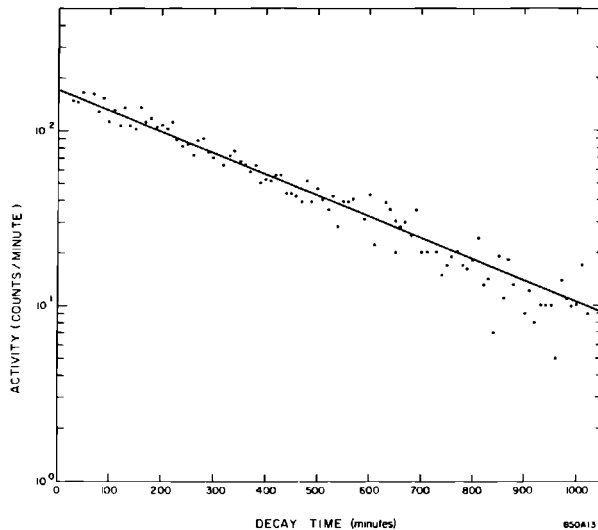
* Thanks are due J. B. McCaslin and the Lawrence Radiation Laboratory, Berkeley, for the use of their facilities and experience.

was then removed and counted on a windowless alpha counter with about 33% of 4π geometry. The 1-hour centrifuge time plus 1-hour wait time before centrifuging was sufficient to allow any short-lived products to decay away and the 4.12-hour ^{149}Tb half-life was followed without ambiguity. Figure 26-13 shows the ^{149}Tb decay from a mercury sample irradiated near a target which was bombarded with 10-GeV electrons. The sensitivity of the system used at Lawrence Radiation Laboratory is such that a 500-g sample irradiated to saturation by a unit flux density gives 3×10^{-2} counts/min.

A few sentences describing how this calibration factor was obtained might be in order. The mercury used in the calibration was placed in a 700-MeV proton beam with gold foils in front and to the rear of the sample. The calibration was then determined relative to gold, assuming that the (n , spallation) cross section is the same as the (p , spallation) cross section.

In the SLAC experiment, the electron beam bombarded a thick target, and a mixture of high-energy particles was incident upon the sample. It was expected that secondary particles would have energies up to that of the incident electron energy, which was 10 GeV. The uncertainties in cross section, plus the fact that the system was calibrated at only one energy, were such that

Figure 26-13 Decay of ^{149}Tb activity in a mercury sample irradiated in the SLAC tunnel near a 10-GeV electron beam targeting in copper. Zero decay time corresponds to 3.5 hours after beam shut off. This allowed for the decay of shorter-lived products and also for the 1-hour centrifuging. The solid line is the slope corresponding to the 4.12-hour half-life of ^{149}Tb .

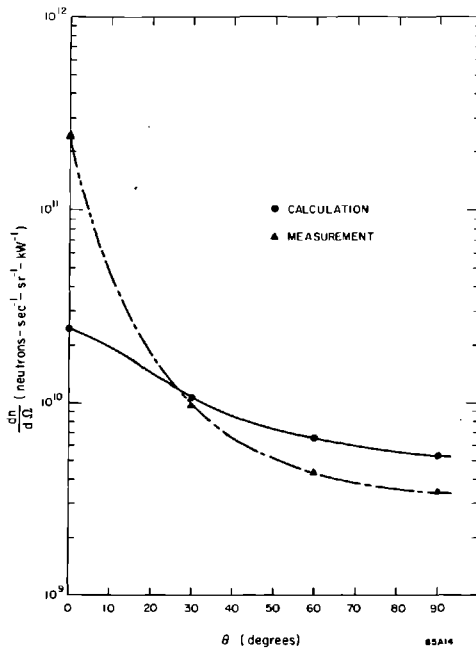


an accurate measurement was improbable, and one had to be satisfied with an order-of-magnitude measurement.

The yield of neutrons with energies above 700 MeV was checked in the forward direction only and compared with the yield of neutrons with energies greater than 25 MeV as measured with the carbon scintillators. With a 10-GeV electron beam incident on a $16X_0$ copper target, the detectors were placed about 5° from beam direction and 10 ft downstream. Twelve inches of lead with a 4-in. hole were located between the target and detectors. From Fig. 26-8, one would estimate the yield of neutrons with energies greater than 700 MeV to be 4.5×10^{11} neutrons/sec-steradian-MW. The measured value, using the mercury detector, was 4×10^{11} neutrons/sec-steradian-MW. With the gross uncertainties in cross section and detector calibration, this is considered excellent agreement.

The yield of neutrons with energies greater than 25 MeV, as measured with the carbon reaction, was 1.4×10^{14} neutrons/sec-steradian-MW which

Figure 26-14 Comparison of measured and calculated values of $dn/d\Omega$ as a function of the angle from the beam direction. The calculations are from Figure 26-8 ($\varepsilon = 25$ MeV). The agreement is good at angles greater than 30° . At 0° , the agreement is poor, due probably to competing reactions.

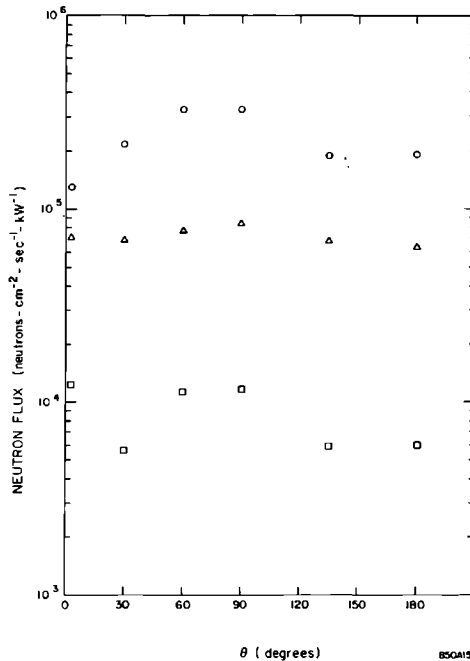


is about 5 times greater than the estimated value of 2.1×10^{13} neutrons/sec-steradian-MW. The high measured value probably indicates the contribution from the (γ, n) reaction.

In another experiment an electron beam of 7 GeV was targeted in end station A in a $16X_0$ copper cylinder ($r_0 = 2.7X_m$) and measurements of neutrons with $E \gtrsim 25$ MeV were made, again using the solid plastic scintillators, at 0° , 30° , 60° , and 90° . In Fig. 26-14, a comparison is made between the measured values at these angles and the calculated curve of Fig. 26-8. As can be seen, there is good agreement at all angles except in the forward direction where the agreement is not expected to be as good due to competing (γ, n) reactions from high-energy photons.

In an effort to generate some information on neutron fluxes in other energy intervals, detectors of bare indium, moderated indium, and aluminum disks were placed at 3° , 30° , 60° , 90° , 135° , and 180° from the beam direction

Figure 26-15 Fast neutron fluxes inside end station A at 20-ft radius from a target bombarded by 7-GeV electrons. Measurements were made using: \circ moderated In foils, \square Al disks, and \triangle bare In foils. Increased fluxes near the 90° direction are probably due to proximity to the end station walls.



in end station A at a radius of 20 ft. An approximate isotropic yield would be expected for neutrons in the giant resonance region, which is the region encompassed by the moderated indium detectors, and partly by the aluminum detectors, and this is, indeed, what was measured. The thermal neutron flux inside the end station should be more or less uniform, for the walls are the main source of thermal neutrons. Figure 26-15 shows the relative fluxes as measured by bare and moderated indium and the aluminum detectors. The flux is isotropic within a factor of about 2.5 and may be even closer to isotropic when the effect of backscatter is added. The detectors at 90° were only 40 ft from the end station walls whereas those at 0° or 180° were at least 100 ft from the end walls. The source strength at 90° , as measured by the moderated indium foils, was about 1.5×10^{12} neutrons/sec-kW which was in good agreement with previous measurements of 1.25×10^{12} neutrons/sec-kW,³⁴ and with calculations.³⁵

Detectors encompassing only three energy intervals make it difficult to unfold a spectrum. However, some information may be presented in a useful manner if one knows the flux of neutrons in each energy range. It was decided to present the data as ratios of fluxes compared to the fluxes as measured by moderated indium foils. This is done in Table 26-2, with the flux of neutrons as measured by Neet¹⁵ at 1-GeV electron energy in the Mark III accelerator also included. Table 26-2 shows that the neutrons measured by the carbon reaction are definitely forward peaked, falling rapidly with increasing production angle, whereas the neutrons measured by the aluminum reaction are essentially isotropic.

Figure 26-9, showing $r^2 D_p$ derived from Fig. 26-8, was checked using a 1-kW electron beam targeted in the middle of end station A. Radiation from the target penetrated different thicknesses of concrete at different angles, giving an excellent check on Fig. 26-9. Neutron measurements were made

Table 26-2 Ratio of neutron source strength measured with aluminum, carbon, or moderated indium, for a 7-GeV electron beam incident on a $16X_0$ copper target^a

Angle	Aluminum <i>moderated indium</i>	Carbon <i>moderated indium</i>	<i>Q (Moderated indium)</i> <i>(neutrons-sec⁻¹kW⁻¹)</i>	
			$E_0 = 7 \text{ GeV}$	$E_0 = 1 \text{ GeV}$
0-3°	0.095	4.96	6×10^{11}	1.95×10^{12}
30°	0.026	0.121	9.9×10^{11}	2.9×10^{12}
60°	0.035	0.036	1.51×10^{12}	4.16×10^{12}
90°	0.035	0.028	1.5×10^{12}	3.82×10^{12}
135°	0.032	—	8.5×10^{11}	4.16×10^{12}
180°	0.031	—	8.8×10^{11}	—

^aThe data at 1 GeV is by Neet (Reference 15).

Table 26-3 Comparison of calculated and measured neutron dose rates around end station A^a

<i>Position</i>	<i>Calculated dose rate (mrem/hour)</i>	<i>Measured dose rate (mrem/hour)</i>
A	45	25
B	9.8	4.9
C	31.2	8.5
D	—	—
E	50	5
F	24	7.8
G	2.8	2.8
H	22	15.8

^a See Fig. 26-5.

outside the end station A walls using a moderated BF₃ detector which detects neutrons in the energy range of from 10 keV to 4 MeV. Figure 26-9 gives no indication of which energy range of neutrons is contributing to the dose outside the walls. Calculations, dividing the neutron flux incident upon the walls into $E_n > 100$ MeV and the giant resonance region, indicate that the high-energy neutrons will contribute almost all the dose outside the walls, even where the wall thickness is only about 3 ft. These high-energy neutrons are moderated in passing through the concrete, and will have an energy distribution different from the incident flux. Evaporation neutrons from the outer parts of the walls would be expected as well as a modified high-energy spectrum. Many, perhaps most, of these neutrons will be in the energy range encompassed by the moderated BF₃ detector. Table 26-3 gives the actual measurements at various locations around end station A (see Fig. 26-5) compared with the expected values as derived from Fig. 26-9. There seems to be reasonable agreement, especially at the larger angles.

26-4 Muon production and attenuation (WRN)

The production and absorption mechanisms for muons are rather well known.³⁶ Because muons essentially lose energy by ionization, a fairly unique range is associated with each energy. At both electron and proton machines the high-energy muons are peaked predominantly in the forward direction because in pair production and in nuclear pion production the transverse momenta are on the order of the particle mass, μ , and the muons are rarely a problem for transverse shielding.²² The muon flux that is produced when a high-energy electron beam is completely attenuated in matter can be calculated by integrating the pair production cross section over the photon distribution in the electromagnetic shower.³⁷ The equations given by Drell³⁸

can be rewritten as the probability per radiation length (in small angle approximation).

$$\frac{d^2\sigma}{d\Omega dE}(E, k, \theta) = \frac{1}{\pi} \left(\frac{m}{E}\right)^2 \frac{\ln(E/\mu)}{\ln(183Z^{-1/3})} \frac{E(k-E)}{k^2} \frac{1}{k} \\ \times \left\{ \frac{k^2 \left[\left(\frac{\mu}{E}\right)^2 + \theta^2 \right]^2 - 2 \left[\left(\frac{\mu}{E}\right)^4 + \theta^4 \right]}{\left[\left(\frac{\mu}{E}\right)^2 + \theta^2 \right]^4} \right\} \\ (\text{GeV-radiation length-steradian})^{-1} \quad (26.7)$$

and

$$\frac{d\sigma}{dE}(E, k) = \left(\frac{m}{\mu}\right)^2 \frac{\ln(E/\mu)}{\ln(183Z^{-1/3})} \frac{1}{k} \left[1 - \frac{4}{3} \frac{E(k-E)}{k^2} \right] \\ (\text{GeV-radiation length})^{-1} \quad (26-8)$$

where

- m = the electron rest mass = 0.511 MeV
- μ = the muon rest mass = 106 MeV
- E = the muon energy
- k = the photon energy
- Z = the atomic number of absorber

Equations (26-7) and (26-8) will probably overestimate the muon yield by a factor of 2 according to Tsai.³⁹

The differential photon track length as given by Rossi¹ under Approximation A of shower theory is

$$\frac{dl}{dk} = 0.57 \frac{E_0}{k^2} (\text{radiation length/GeV}) \quad (26-9)$$

A Monte Carlo study of the longitudinal development of electron-photon cascade showers in copper has been done by Zerby and Moran⁹ where the track length results are compared with Eq. (26-9). The approximate analytic results fit the Monte Carlo data rather well for photons in the energy range below $0.6 E_0$ and above the critical energy for copper (≈ 20 MeV).

DeStaebler⁴⁰ has made a comparison of several track length formulas with the Monte Carlo data. Figure 26-16 shows two of these track length formulas divided by the Approximation A result,¹ Eq. (26-9), as a function of $u = k/E_0$. The simple Approximation A is good to within a factor of 2 except perhaps at the very tip. Equation (26-9) is used in the present calculation with the understanding that the results should give a conservative estimate of muon fluxes for shielding purposes.

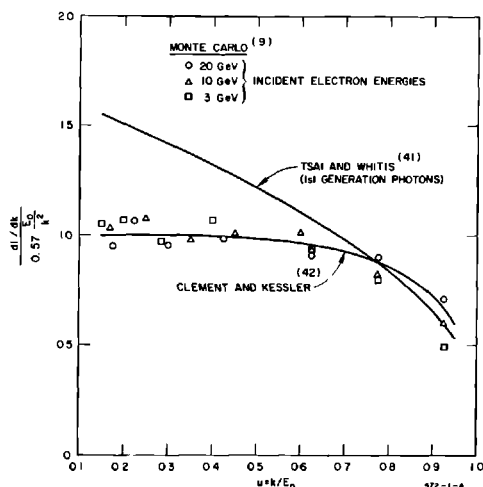


Figure 26-16 Differential photon track length divided by Approximation A (Reference 1) versus the fractional photon energy, $u = k/E_0$.

The differential muon flux a distance R from the target is

$$\frac{d\Phi}{dE}(E_0, E, \theta) = \frac{2I}{R^2} \int_E^{E_0} \frac{d^2\sigma}{d\Omega dE} \frac{dl}{dk} \text{ (muon/cm}^2\text{-sec-GeV)} \quad (26-10)$$

where I = electron current (e^-/sec) and where the factor of 2 comes from the fact that both μ^+ and μ^- are required. The result of this integration is

$$\frac{d\Phi}{dE}(E_0, E, \theta) = \frac{2IE_0 0.57 \ln\left(\frac{E}{\mu}\right) \left(\frac{m}{\mu}\right)^2}{R^2 \mu^2 \pi (1 + \eta^2)^2 \ln(183Z^{-1/3})} H(E_0, E, \theta) \quad (26-11)$$

where

$$H(E_0, E, \theta) = \frac{1 - x^2}{2} - \frac{1}{6} \left[1 - 4x^3 \left(1 - \frac{3}{4}x \right) \right] \left[\frac{1 + \eta^4}{(1 + \eta^2)^2} \right] \quad (26-12)$$

and where $x \equiv E/E_0$, $\eta \equiv \theta/\theta_0$, and $\theta_0 \equiv \mu/E$.

The integral muon flux is

$$\Phi(E_0, E, \theta) = \int_E^{E_0} \frac{d\Phi}{dE} dE \quad (26-13)$$

from Eqs. (26-11) and (26-12). The integration was performed numerically on the B5500 computer using the procedure SIMPS6.* Form factor effects are neglected, as is multiple scattering.

* This program was written and developed by J. Welsch of SLAC.

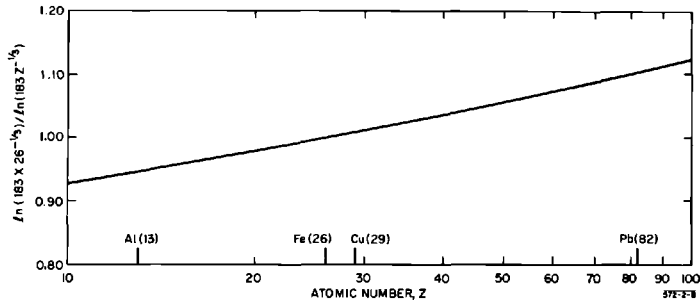
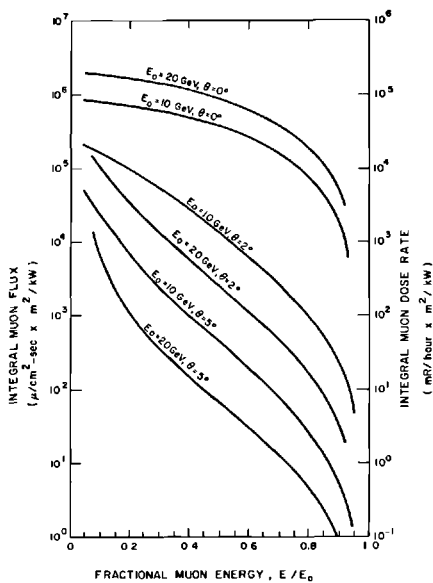


Figure 26-17 Curve showing the slight dependence of the muon flux on the atomic number, Z .

To convert flux to dose rate, it seems reasonable to use the simple conversion factor $1 \mu/\text{cm}^2\text{-sec} = 0.1 \text{ mrem/hour}$, which corresponds to a quality factor (QF) of 1 and an energy loss of $1.75 \text{ MeV/g}\cdot\text{cm}^{-2}$.

The Z -dependence of the target material enters in the form $\ln(183Z^{-1/3})$. All these calculations have been done with $Z = 26$ (Fe), and Fig. 26-17 gives the necessary multiplicative factor for other absorbers.

Figure 26-18 The integral muon flux (for 1 kW at 1 meter) versus the fractional muon energy, E/E_0 , for several production angles and incident electron beam energies.



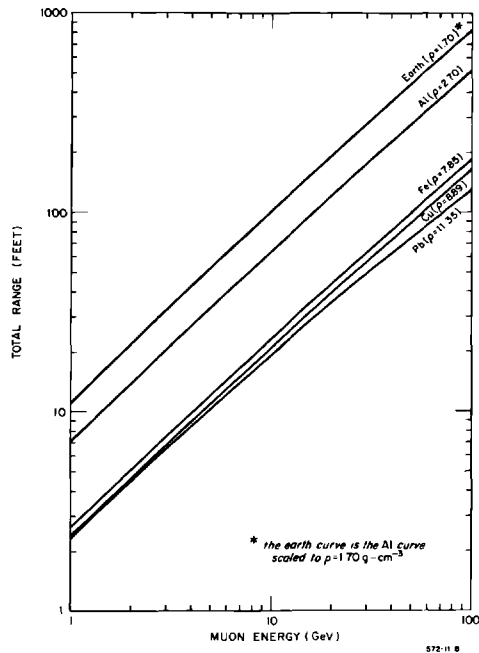


Figure 26-19 Range energy curves for muons in various shielding materials.

The results of the calculation are shown in Fig. 26-18 where both the integral flux and dose rate for $R = 1$ meter and $P = 1$ kW are plotted against the ratio E/E_0 for various values of θ and E_0 . In order to calculate the muon flux, one needs to know the lower limit on the muon energy, which is determined by the shielding between the source and the observer. Since multiple scattering has not been included, the calculation will overestimate the flux when thick shields are close to the source. For thick shields at large distances from the source, the calculation should be better since the production angle dominates over the multiple scattering.

A set of range-energy curves for muons in various materials is given in Fig. 26-19 which aid in doing shielding calculations. The curves represent an extension of previous calculations to higher energies and include pair production, bremsstrahlung, and nuclear interaction losses.^{43,44} A similar calculation has been done by Thomas.⁴⁵

Integration of the flux over 4π steradians results in the total muon yield shown in Fig. 26-20. Also shown is the yield of muons from a high-energy proton beam⁴⁶, which is richer at lower energies partly because lower-energy pions are more likely to decay.

Multiple scattering is also important when the shield is thick but narrow, for then the muon flux can readily escape the sides. A calculation has been made⁴⁷ which accounts for the energy loss in the medium in which the

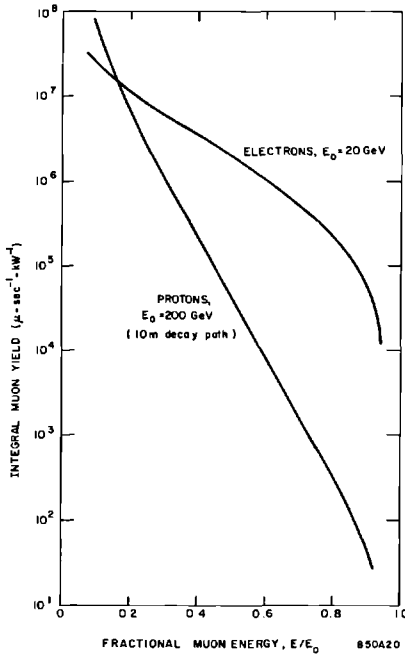


Figure 26-20 Integral muon yield versus the fractional muon energy for incident 20-GeV electrons. Also included for comparison is the muon yield (from pion decay) that is expected from a 200-GeV proton beam.

multiple elastic scattering takes place. The defining equation is the Fermi diffusion equation¹, which has been solved by Eyges⁴⁸ with energy loss considered. A second-order polynomial is fitted to existing range-momentum data,⁴⁹ and the integral expressions of Eyges are numerically integrated to obtain y_{rms} and θ_{rms} .

The root-mean-square lateral displacement and scattering angle, due to multiple scattering of muons in iron and silicon dioxide for incident momenta of 5, 10, and 20 GeV/c, are shown in Figs. 26-21 and 26-22, respectively.

If we neglect energy loss (i.e., $p\beta = \text{constant}$), the mean square values are

$$\langle \theta^2 \rangle = \frac{1}{2} \left(\frac{E_s}{p\beta} \right)^2 t \tag{26-14}$$

and

$$\langle y^2 \rangle = \frac{1}{6} \left(\frac{E_s}{p\beta} \right)^2 t^3 \tag{26-15}$$

where t = depth of penetration in radiation lengths, and $E_s = 21.2$ MeV.

This special case is compared in Figs. 26-21 and 26-22 for $p\beta = 20$ GeV/c and for SiO_2 .

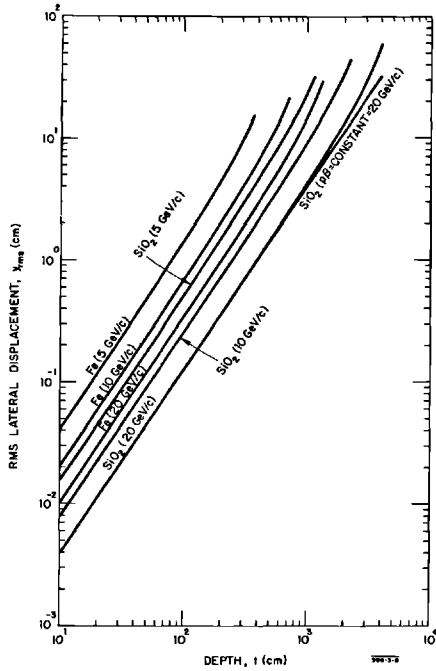


Figure 26-21 Root-mean-square lateral displacement due to multiple elastic scattering of muons of various incident momenta in iron and silicon dioxide.

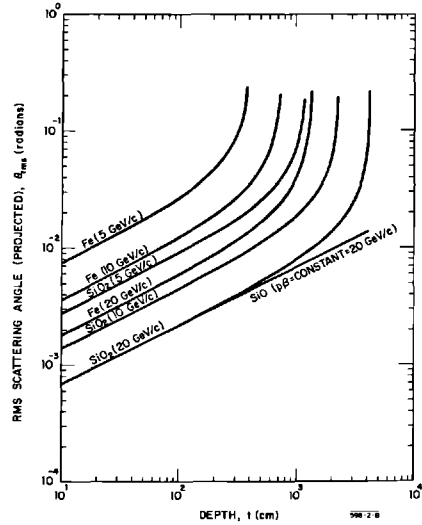


Figure 26-22 Root-mean-square projected angle due to multiple elastic scattering of muons of various incident momenta in iron and silicon dioxide.

26-5 Radiation in the 2-mile tunnel and penetrations (HDeS, TMJ)

Dose determination

In general, the flux at a point in a duct (penetration) consists of a direct part which decreases as $1/z^2$ and a part that has scattered off the walls (depending upon albedo) and decreases faster than $1/z^2$, z being the distance up the duct. The fractional transmission, $g(z)$, in a cylindrical duct for a parallel flux of neutrons is given by⁵⁰

$$g(z) = \frac{\phi(z)}{\phi(0)} = \left(\frac{a}{z}\right)^2 \left[1 + K \frac{a}{z}\right] \quad \text{for } 4 < z/a < 36 \quad (26-16)$$

where

a = the radius of the cylindrical duct

$K = 60$ for photons and thermal neutrons, and closer to 16 for fast neutrons

$\phi(z)$ = the flux at a point z in the duct

$\phi(0)$ = the flux at the entrance to the duct

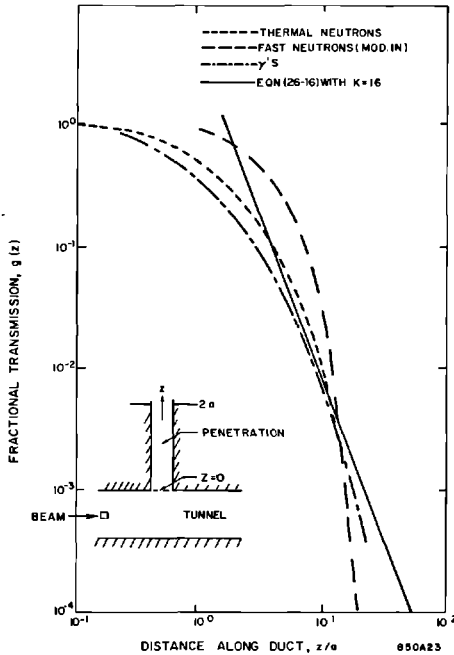


Figure 26-23 Fractional transmission of neutrons and photons in a duct. Measurements of thermal and fast neutrons and photons are shown along with the calculated transmission taken from Eq. (26-16), with $K = 16$. The source was a thick copper target bombarded with 1-GeV electrons.

The fractional transmission has been measured for thermal neutrons by other authors⁵¹ and is shown in Fig. 26-23 which was used in calculating the dose rate at the top of the penetrations at SLAC. The PuBe neutrons closely follow the same curve when measured in a 27-in. diameter service penetration.

The original calculation of DeStaeblcr,⁵⁰ assuming a line source, gave the result

$$D(\text{mrem/hour}) = 3.6 \times 10^6 Fg(z)\phi(0) \tag{26-17}$$

where

- D = the dose rate at the end of a penetration
- 3.6×10^6 = a factor which converts rem/sec to mrem/hour
- F = the biological effect per fast neutron (3.8×10^{-8} rem/neutron-cm⁻²)
- g = the transmission in the duct; for $z/a = 21$ as in the case of a service penetration, $g = 10^{-3}$ from Fig. 26-23
- $\phi(0)$ = the fast neutron flux at the bottom of a penetration

A measurement was made at the end of the first 660 ft of accelerator. A 1-GeV, 1.25-kW electron beam was completely absorbed in a target located 16.1 ft from a penetration. Using a source strength of 1.25×10^{12} neutrons/sec-kW radiating isotropically,³⁴ one obtains

$$D = (3.6 \times 10^6)(3.8 \times 10^{-8})(10^{-3}) \left(\frac{1.25 \times 10^{12}}{4\pi(16.1 \times 30.5)^2} \right)$$

$$= 56 \text{ mrem/hour}$$

The measured value was 60 mrem/hour for the above conditions, which agrees with the calculation.

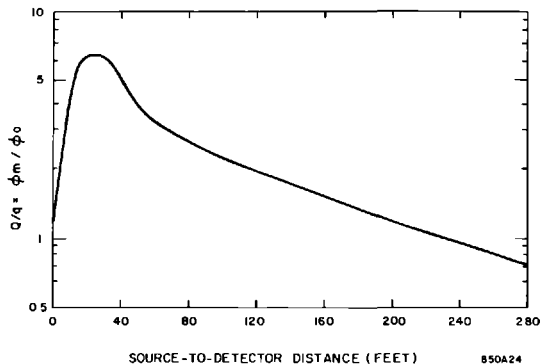
The fractional transmissions, $g(z)$, in a 28-in diameter service penetration were measured for thermal neutrons, fast neutrons, and photons, and are included in Fig. 26-23. The photons entering the 28-in. service penetration are essentially parallel; transmission in a penetration upstream of the target was the same as that downstream.

A different situation exists when a source is placed inside a tunnel and the flux is measured down that same tunnel, such as the case when a beam targets somewhere in the accelerator housing. The high-energy component will be peaked in the forward direction. The giant resonance neutrons, which are isotropic, should give a result similar to a PuBe source suspended in the tunnel. If there were no scattering effects, the flux should decrease according to

$$\phi_0 = \frac{q}{4\pi r^2} \quad (26-18)$$

where r is the straight line distance from the source to the detector, and q is the

Figure 26-24 Transmission of Pu-Be neutrons in the accelerator tunnel [$q = \text{constant}$, $Q = Q(r)$].



neutron source strength. An effective source strength, Q , can be defined in terms of the actually observed flux, ϕ_m , by

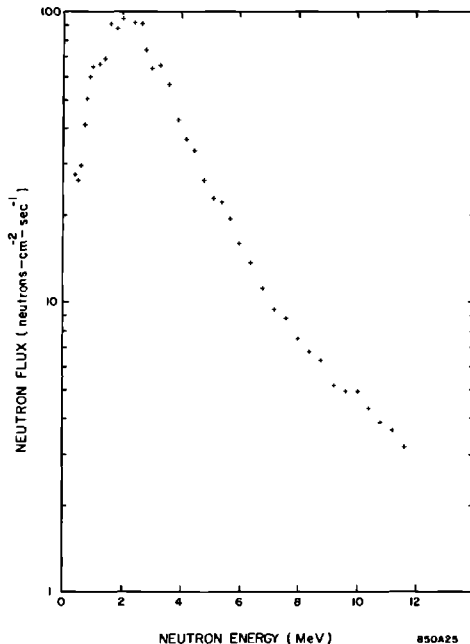
$$\phi_m = \frac{Q}{4\pi r^2} \quad (26-19)$$

and Fig. 26-24 shows $(\phi_m/\phi_0) = (Q/q)$ as a function of r for PuBe neutrons measured in the tunnel. The variation of $Q(r)$ seems plausible. If r is small compared with the cross-sectional dimensions of the tunnel, then $Q \approx q$; at $r \approx 20$ ft, Q builds up to a maximum of about $5q$, presumably owing to scattering from the walls of neutrons that would otherwise never have hit the counter; for r greater than a couple of hundred feet, Q decreases roughly exponentially with a mean free path corresponding to the ≈ 1 -MeV scattering cross section in air.

Determination of the neutron spectrum in the penetrations

Nuclear track emulsion (Ilford L4) was placed at the top of a 28-in. service penetration which was located approximately 10 ft downstream from a target. Two inches of lead was placed around the emulsion in order to reduce the γ -radiation level. The beam energy was 10 GeV and the target was 9 in.

Figure 26-25 Neutron energy spectrum in a SLAC penetration near a target that is being struck by 10-GeV electrons.



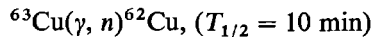
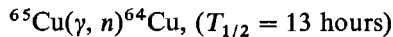
of water-cooled copper. The processing and scanning of the emulsion, and the emulsion itself, were provided by the Health Physics Department of the Lawrence Radiation Laboratory in Berkeley, California. They also obtained the neutron spectrum from the proton recoil data using their computer codes RECOIL I and RECOIL DD.⁵² The resultant spectrum is shown in Fig. 26-25. The peak at 2 MeV is not unexpected since the giant resonance spectrum should dominate with such a shielding geometry.

26-6 Residual radiation (TMJ)

Beam loss along the accelerator is estimated to be 3% of the final beam power.²² This occurs primarily in the thirty beam scrapers and small couplings along the machine. There will be times, especially during tune-up, when local points will intercept more of the beam. An example of this was seen during initial operations on the 660-ft accelerator where, using moderated indium foils to measure the neutron flux, an apparent beam power loss of 8.7% was noted in the collimator at the end of Sector 1.

The accelerator problems are typical, with activation occurring in metal parts, concrete walls, water, and air. In concrete, the principal reaction of concern is $^{23}\text{Na}(n, \gamma)^{24}\text{Na}$ with $T_{1/2} = 15$ hours. In certain areas, activation of the concrete is a significant portion of the radiation inside the tunnel. Boron frit (B_2O_3) has been added to the concrete walls near the positron target and in the beam switchyard; the effectiveness⁵³ is shown in Fig. 26-26.

Along the accelerator waveguide, the principal reactions are



with ^{58}Co ($T_{1/2} = 71$ days) and ^{60}Co ($T_{1/2} = 5.3$ yr) becoming important daughter products after long irradiation times, and long (>100 hours) waiting times. Calculations of residual activity are made from the yield formula,⁵⁴

$$R(\text{curies}) = 58 g \left(\frac{X_0}{A} \right) \int \frac{\sigma dk}{k^2} \text{ per MW of incident beam}$$

where

- g = the fractional atomic abundance of parent nuclide
- X_0 = the radiation length in grams per square centimeter
- A = the atomic weight of the material
- $\sigma(k)$ = the cross section in microbarns

Tables 26-4 and 26-5 show some of the radioactive products that will be formed from copper.

For a uniform 3% of 2.4-MW beam power loss along the accelerator and for 10^2 to 10^4 hours irradiation times, the predicted levels inside the tunnel as a function of waiting time are shown in Fig. 26-27.

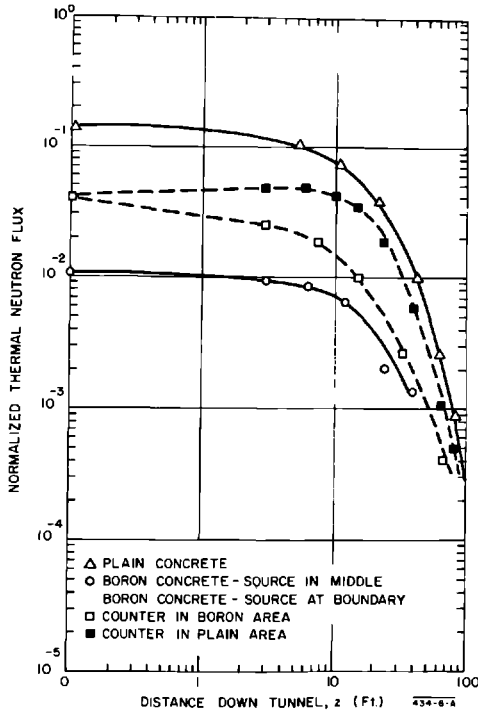


Figure 26-26 Normalized thermal neutron flux versus distance down the accelerator tunnel showing the effect of adding boron to concrete.

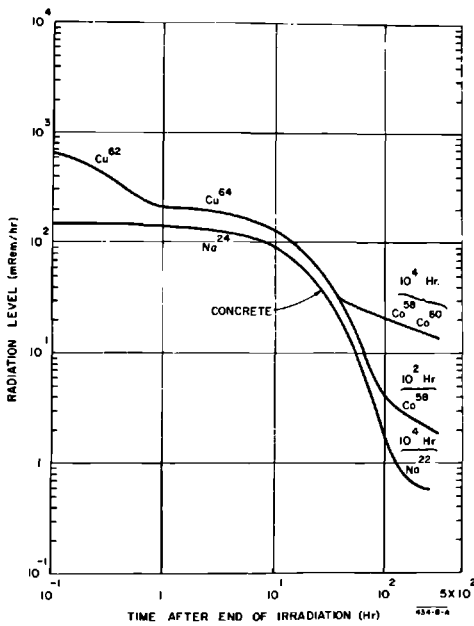


Figure 26-27 Radiation levels in the accelerator tunnel versus waiting time for 10^2 and 10^4 hours irradiation time. SLAC worker tolerance is 0.75 mrem/hour.

Table 26-4 Photon-induced activities in copper

Daughter nuclide element	A	Mean life τ (hour)	Radiation (γ energy) in MeV	E_γ (MeV)	Yield relative ^a to ⁶² Cu	RE_γ (Energy) \times (Activity) ^b (MeV-Ci)
Cu	64	18.4	β^+, β^-	0.60	0.58	390.0
	62	0.23	$\sim 2\% \gamma, \beta^+$	1.10	1.00	1230.0
	61	4.8	$\sim 10\% \gamma, \beta^+$	0.94	0.18	190.0
Ni	57	52.0	1.4, 1.9, β^+	1.99	1.8×10^{-3}	4.0
Co	60	6.6×10^4	1.17, 1.33	2.51	(2.0×10^{-2})	56.0
	58	2.5×10^3	0.80, β^+	0.94	(2.7×10^{-2})	28.0
	56	2.7×10^3	0.89, others, β^+	0.70	(1.2×10^{-2})	9.4
	55	26.0	Many, β^+	2.02	8.5×10^{-4}	1.9
Fe	59	1.56×10^3	1.1, 1.3	1.29	(3.0×10^{-3})	4.3
Mn	56	3.7	0.8, 2.8	1.80	3.0×10^{-3}	6.1
	54	1.0×10^4	0.8	0.84	(5.0×10^{-3})	4.7
	52	2.0×10^2	1.4, β^+	2.45	1.3×10^{-3}	3.6
	51	1.1	β^+	1.02	(1.2×10^{-3})	1.4

^a Parentheses indicate that yield is inferred, not measured; Reference 55.

^b For a power absorption of 3% of 2.4 MW.

An ionization chamber lowered down various service penetrations gives a beam loss profile during machine operation. Figure 26-28 is typical for an early period of operation. This profile was a function of many variables, such as focusing, steering, phasing, and so on. Residual activity profiles follow the same shape, with the beam scrapers and small flexible couplings being the main hot spots. After absorbing 1 kW of beam power, levels 2 ft away from a copper target with 2 in. of lead shielding are typically a few roentgen per hour, 5 min after beam shutoff. Levels in the aisle along the accelerator vary from 0.1 mR/hour to over 1 R/hour, and decrease by an order of magnitude within the first 8 hours.

Table 26-5 Activities in copper induced by neutrons

Reaction	Mean life τ (hour)	Radiation (γ energy) in MeV	E_γ (MeV)	(Energy) \times (Activity) RE_γ (MeV-Ci)
⁶⁵ Cu(<i>n</i> , 2 <i>n</i>) ⁶⁴ Cu	18.4	β^+, β^-	0.60	20.0
(<i>n</i> , <i>p</i>) ⁶⁵ Ni	3.7	1.1, 1.4	0.59	2.8
(<i>n</i> , α) ⁶² Co	0.34	≈ 1.2	≈ 1.3	—
⁶³ Cu(<i>n</i> , 2 <i>n</i>) ⁶² Cu	0.23	$\sim 2\% \gamma, \beta^+$	1.10	80.0
(<i>n</i> , <i>p</i>) ⁶³ Ni	$\sim 10^6$	0.0	0.0	0.0
(<i>n</i> , α) ⁶⁰ Co	6.6×10^4	1.17, 1.33	2.51	—

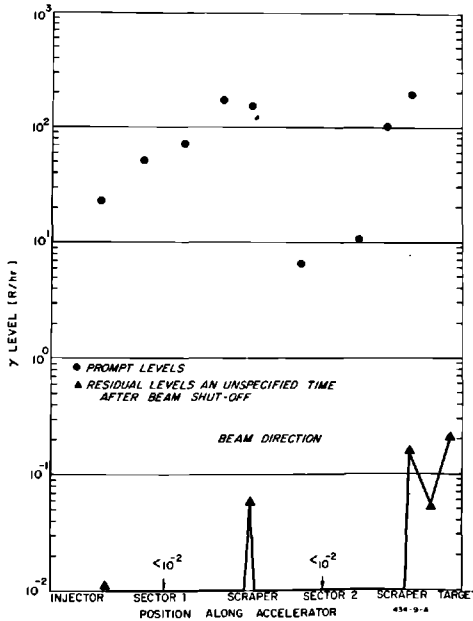


Figure 26-28 A typical beam loss profile for the tune-up period on the 660-ft accelerator as measured with an ionization chamber. Residual activity follows the prompt radiation curve and is primarily localized to beam scrapers and the target. The copper target has a 2-in. Pb jacket around it.

Cooling water along the accelerator, and especially in the slits, collimators, and beam dumps, will become radioactive. Typical levels in the water of a dump^{56,57} when irradiated to saturation with 1 MW of beam power are shown in Table 26-6. Water at a heat exchanger associated with beam switchyard components was measured and the radioactive levels were in agreement

Table 26-6 Activity in water^a

Daughter nuclide	R (Ci)	Mean life τ (hours)
^{15}O	35,000	0.05
^{13}N	1,390	0.24
^{11}C	1,390	0.5
^7Be	280	1.85×10^3
^3H	400	1.55×10^5

^a Irradiated to saturation with 1 MW of beam power

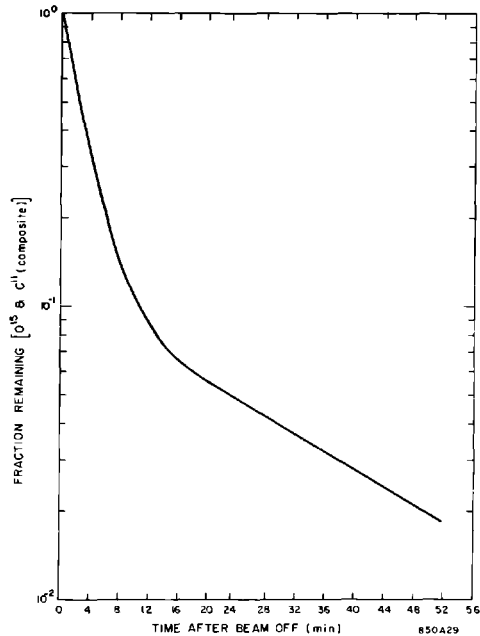


Figure 26-29 Decay of radioactive water at beam switchyard service areas. Half-lives are those of ^{15}O and ^{11}C .

with the predicted values, with the exception of ^{13}N , which was absent. Figure 26-29 shows the decay of the radioactive water as a function of time. It is apparent that this water presents a significant hazard to health and must be carefully shielded and monitored (see Chapter 21). The radioactive water of each unit is contained within a closed loop, with nonradioactive water cooling in a heat exchanger outside the main earth shield. Water in the radioactive side of the loop is monitored on a sampling basis, whereas the nonradioactive water is monitored continuously for ruptures, etc. to ascertain that no significant amounts of radioactivity reach the cooling tower and from there the outside world.

Radioactive and chemically active air produced inside the tunnel presents a significant hazard to personnel. Using a 3% beam power loss uniformly distributed along the accelerator, DeStaeblér⁵⁸ has calculated the rate of formation of noxious chemicals in the tunnel to be about 1 ppm/day. For radioactive air, the following reactions are of concern⁵⁹: $^{14}\text{N}(\gamma, n)^{13}\text{N}$, $^{14}\text{N}(n, 2n)^{13}\text{N}$, $^{16}\text{O}(\gamma, n)^{15}\text{O}$, with $^{40}\text{A}(\gamma, p)^{39}\text{Cl}$ and $^{14}\text{N}(\gamma, 2np)^{11}\text{C}$ also of importance. The equilibrium concentrations in the tunnel are shown in Table 26-7. From this it is calculated that if a person enters the tunnel immediately after beam shutoff and remains for a period significantly long compared with the half-lives of the nuclides involved, he would receive a total

Table 26-7 Equilibrium concentrations of final nuclides after irradiation of air

<i>Final nuclide</i>		<i>Rate of formation R (nuclides/sec)</i>	<i>Equilibrium concentration in tunnel ($\mu\mu\text{Ci/cm}^3$)</i>
^{11}C		0.24×10^{10}	3.1
^{13}N	Incident γ	12.0×10^{10}	
	Incident n	$<3.0 \times 10^{10}$	
	Total	15.0×10^{10}	190.0
^{15}O		17.0×10^{10}	220.0
^{39}Cl		0.42×10^{10}	5.5

exposure of 97 mrem from radioactive gas. A wait time of 20 min before entry would decrease this to 20 mrem. To reduce further this hazard, the tunnel, which is normally sealed from the outside world, is first vented before entry is permitted. During venting, one complete air change occurs approximately every 10 min.

26-7 Outline: order-of-magnitude shielding calculations (TMJ, WRN)

A. Attenuation of the electron-photon shower

1. The longitudinal shower decreases exponentially with an absorption mean free path, Λ , given in Fig. 26-1. The shower maximum occurs at a depth of about $4X_0$ for $E_0 = 1$ GeV and about $10X_0$ for $E_0 = 20$ GeV.
2. The fraction of incident energy (power) that escapes radially can be found using Fig. 26-2, which plots the radius in Moliere units, X_m . Both X_0 and X_m are given in Fig. 26-1. Figure 26-2 is independent of both E_0 and the absorbing material.

B. Photon production and attenuation

1. Use Fig. 26-3 to determine the unshielded photon dose rate coming from a thick target ($t \approx 15X_0$, $r_0 \approx 3X_m$) as a function of angle.
2. Determine the effective photon energy from the minimum in the mass absorption curve (good geometry) for the target material.
3. Determine the absorption coefficient for this energy in the shielding material.
4. Use $D = D_0 e^{-\mu t}$, where D_0 is the unshielded dose rate, μ is the absorption coefficient, t is the shield thickness, and D is the required dose rate.
5. This method is not good for angles less than 10° .

C. Neutron production and attenuation

1. Calculate the shield thickness, H , in feet of earth equivalent ($\rho = 1.7 \text{ g-cm}^{-3}$).
2. Determine the neutron dose rate through the shield from Fig. 26-9.
3. This estimate should be good to a factor of 2 for angles greater than about 30° .

D. Muon production and attenuation

1. Determine the lowest muon energy, E , by using the shield thickness and Fig. 26-19.
2. With E/E_0 , look for the muon dose rate on Fig. 26-18.
3. Divide this dose rate by 2 since the cross section given by Tsai³⁹ is approximately half as large as that given by Drell.³⁸
4. This estimate might be as much as 5 times too high since nuclear form factors and multiple scattering have been neglected.

E. Radiation through penetrations and holes in shields

1. Use Fig. 26-23 to determine the transmission, $g(z)$.
2. Use $D(z) = D(0)g(z)$ to determine the dose rate at the end of the duct, $D(z)$, with a prior knowledge of the dose rate at the entrance to the duct, $D(0)$.

26-8 General discussion (TMJ, WRN)

The preceding sections describe the various shielding calculations and measurements that have been made at SLAC to date (July 1967). A number of subjects have been intentionally omitted, either because the measurements have not been adequately related to theory or because they are too extensive to cover sufficiently in this chapter. A few general statements might be of practical interest, however.

It has been found that Eq. (26-14) does not adequately describe the spread of primary electron beams in thin targets because large-angle scattering turns out to be significant. It is necessary to go to more elaborate theory⁶⁰ in order to determine the effective beam cone for shielding purposes.

In areas where roof shielding is thin or contains voids or holes, there will be a component of radiation, both neutrons and photons, that scatters off the atmosphere. This skyshine problem exists at SLAC and is being studied. Similarly, the problem of radiation scattering through a maze is also being looked at. A general rule-of-thumb has been found to work for both photon and neutron radiation, namely, one gets about a factor of 20 reduction with each 90° bend in a thick concrete maze.

References

- 1 B. Rossi and K. Greisen, *Rev. Mod. Phys.* **13**, 240 (1941); B. Rossi, *High-Energy Particles*, Prentice-Hall, Engelwood Cliffs, New Jersey, 1952.
- 2 S. Z. Belenkii and I. P. Ivanenko, *Soviet Phys.-Usp.* **2**, 912 (1960).
- 3 Y. Murata, *J. Phys. Soc. Japan*, **20**, 209 (1965).
- 4 G. Backenstoss, B. D. Hyams, G. Knop, and U. Stierlin, *Nucl. Instr. Methods* **21**, 155 (1963).
- 5 W. Blocker, R. W. Kenney, and W. K. H. Panofsky, *Phys. Rev.* **79**, 419 (1950).
- 6 T. Rockwell, III (Ed.), *Reactor Shielding Design Manual*, p. 447, Van Nostrand, New York, 1956.
- 7 K. Kamata and J. Nishimura, *Progr. Theoret. Phys. (Kyoto)*, Suppl. No. 6, 93 (1958).
- 8 H. H. Nagel, *Z. Physik.* **186**, 319 (1965); [English Transl., Rept. No. SLAC-TRANS-28, Stanford Linear Accelerator Center, Stanford University, Stanford, California (1965)].
- 9 C. D. Zerby and H. S. Moran, *J. Appl. Phys.* **34**, 2445 (1963); "Studies of the Longitudinal Development of High-Energy Electron-Photon Cascade Showers in Copper," Rept. No. ORNL-3329, Oak Ridge National Laboratory, Tennessee (1962); and "A Monte Carlo Calculation of the Three Dimensional Development of High-Energy Electron-Photon Cascade Showers," Rept. No. ORNL-TM-422, Oak Ridge National Laboratory, Tennessee (1962). Also, private communication.
- 10 U. Völkel, "Elektron-Photon-Kaskaden in Blei für Primärteilchen der Energie 6 GeV," Rept. No. DESY 65/6, Deutsches Elektronen-Synchrotron, Hamburg, Germany (1965); [English Transl., Rept. No. SLAC-TRANS-41, Stanford Linear Accelerator Center, Stanford University, Stanford, California (1966)].
- 11 A. Kantz and R. Hofstadter, *Phys. Rev.* **89**, 607 (1953); *Nucleonics* **12**, 36 (March 1954).
- 12 W. R. Nelson, T. M. Jenkins, R. C. McCall, and J. K. Cobb, *Phys. Rev.* **149**, 201 (1966).
- 13 K. Greisen, "The extensive air showers," *Progr. Elem. Particle Cosmic Ray Phys.*, **3**, 22 (1956).
- 14 O. I. Dovzhenko and A. A. Pomanskiĭ, *Soviet Phys.-JETP* **18**, 187 (1964).
- 15 D. A. G. Neet, "Radiation Exposure in the Switchyard," Rept. No. SLAC-TN-65-9, Stanford Linear Accelerator Center, Stanford University, Stanford, California (1965).
- 16 F. H. Attix, "Present Status of Dosimetry by Radiophotoluminescence and Thermoluminescence Methods," Rept. No. NRL Report 6145, Naval Research Laboratory, Washington, D.C. (September 1964).
- 17 B. J. Moyer, "Evaluation of Shielding Required for the Improved Bevatron," Rept. No. UCRL-9769, Lawrence Radiation Laboratory, Berkeley, California (June 1961).
- 18 Roger Wallace, *Nucl. Instr. Methods* **18**, **19**, 405 (November 1962).

- 19 U.S. National Bureau of Standards, "Protection against neutron radiation up to 30 MeV," *Natl. Bur. Std. (U.S.) Handbook* 63, (November 1957).
- 20 International Commission on Radiological Protection, "Protection against electromagnetic radiation above 3 MeV and electrons, neutrons and protons," *ICRP Publ. No. 4*, p. 4, Pergamon, New York, 1964.
- 21 U.S. National Bureau of Standards, "Shielding for high-energy electron accelerator installations," *Natl. Bur. Std. (U.S.) Handbook* 97 (July 1964).
- 22 H. DeStaebler, Jr., "Transverse Radiation Shielding for the Stanford Two-Mile Accelerator," Rept. No. SLAC-9, Stanford Linear Accelerator Center, Stanford University, Stanford, California (November 1962).
- 23 A. Wattenberg, "Nuclear reactions at high energies," in *Encyclopedia of Physics*, Vol. XL, p. 450, Springer, Berlin, 1957.
- 24 M. E. Toms, "Bibliography of Photo- and Electronuclear Disintegrations," Rept. No. NRL-BIB-24, U.S. Naval Research Laboratory, Washington, D.C. (July 1965).
- 25 V. I. Antonesoc, "Photonuclear Reactions," *Bibliographical Series No. 10*, International Atomic Energy Agency, Vienna (1964).
- 26 Charles E. Roos and V. Z. Peterson, *Phys. Rev.* **124**, 1610 (1961).
- 27 H. R. Crouch *et al.*, *Phys. Rev. Letters* **13**, 636 (1964).
- 28 H. S. Murdoch and H. D. Rathgeber, *Phys. Letters* **13**, 267 (1964).
- 29 S. J. Lindenbaum, "Shielding of high-energy accelerators," *Ann. Rev. Nucl. Sci.* **11**, 213 (1961).
- 30 S. Kao and G. Voss, "Effectiveness of Ilmenite-Loaded Concrete in Attenuating Neutron Radiation Produced by a 5-BeV Photon Beam," Rept. No. CEAL-1007, Cambridge Electron Accelerator, Cambridge, Massachusetts (December 1963).
- 31 St. Charalambus, J. Dutrannois, and K. Goebel, "Particle Flux Measurements with Activation Detectors," Rept. No. CERN/DI/HP-90, European Council for Nuclear Research, Geneva (1966).
- 32 J. B. McCaslin, H. Wade Patterson, Alan R. Smith, and Lloyd D. Stephens, "Some Recent Developments in Technique for Monitoring High-Energy Accelerator Radiation," Rept. No. UCRL-16769, Lawrence Radiation Laboratory, Berkeley, California (1966).
- 33 E. M. Franz and G. Friedlander, *Nucl. Phys.* **67**, 123 (1966).
- 34 H. DeStaebler, T. Jenkins, W. R. Nelson, "Reduction of the Thermal Neutron Flux in Concrete Using Paraffin Moderators," Rept. No. SLAC-TN-65-11, Stanford Linear Accelerator Center, Stanford University, Stanford, California (1965).
- 35 K. G. Dedrick and H. H. Clark, "Photoneutron Yields from Excitation of the Giant Resonance," Rept. No. M-225, Stanford Linear Accelerator Center, Stanford University, Stanford, California (1960).
- 36 G. N. Fowler, and A. W. Wolfendale, "The interaction of μ -mesons with matter," *Progr. Elem. Particle Cosmic Ray Phys.* **4**, 107 (1958).

- 37 W. R. Nelson, "Muon Production Calculations for Muon Shielding," Rept. No. SLAC-TN-66-37, Stanford Linear Accelerator Center, Stanford University, Stanford, California (1966).
- 38 S. Drell, "Some Aspects of Target Area Design for the Proposed Stanford Two-Mile Linear Electron Accelerator," Rept. No. M-200, Section M-200-7A, W. W. Hansen Laboratories, Stanford University, Stanford, California (Summer 1960).
- 39 Y. S. Tsai, "Estimates of secondary-beam yields at SLAC," *SLAC Users Handbook*, D.3-3, Stanford Linear Accelerator Center, Stanford University, Stanford, California.
- 40 H. DeStaebler, private communication, Stanford Linear Accelerator Center, Stanford University, Stanford, California (July 1966).
- 41 Y. S. Tsai and Van Whitis, *Phys. Rev.* **149**, 1248 (1966).
- 42 G. Clement and P. Kessler, *Nuovo Cimento* **37**, 876 (1965); G. Clement, *Compt. Rend.* **257**, 2971 (November 1963).
- 43 W. H. Barkas and M. J. Berger, "Tables of Energy Losses and Ranges of Heavy Charged Particles," NASA-SP-3013, National Aeronautics and Space Administration, Washington, D.C. (1964).
- 44 P. J. Hayman, N. S. Palmer and A. W. Wolfendale, *Proc. Roy. Soc. (London)* **A275**, 391 (1963).
- 45 R. H. Thomas, private communication, Lawrence Radiation Laboratory, Berkeley, California (July 1964).
- 46 "200 BeV Accelerator Design Study," Rept. No. UCRL-16000, Lawrence Radiation Laboratory, Berkeley, California (June 1965).
- 47 W. R. Nelson, "Multiple Elastic Scattering of Muons with Energy Loss," Rept. No. SLAC-TN-66-41, Stanford Linear Accelerator Center, Stanford University, Stanford, California (1966).
- 48 L. Eyges, *Phys. Rev.* **74**, 1534 (1948).
- 49 W. H. Barkas, "The Range-Energy Function," Rept. No. UCRL-10292, Lawrence Radiation Laboratory, Berkeley, California (August 21, 1962).
- 50 H. DeStaebler, "Radiation Problems Arising from Holes in the Transverse Shielding," Rept. No. SLAC-TN-62-71, Stanford Linear Accelerator Center, Stanford University, Stanford, California (1962).
- 51 B. T. Price, C. C. Horton, and K. T. Spinney, *Radiation Shielding*, Macmillan (Pergamon) New York, 1957.
- 52 R. L. Lehman and O. M. Fekula, *Nucleonics* **22** (No. 11), 35 (1964).
- 53 H. DeStaebler and T. Jenkins, "Pu-Be Neutron Measurements in the Accelerator Tunnel," Rept. No. SLAC-TN-65-24, Stanford Linear Accelerator Center, Stanford University, Stanford, California (1965).
- 54 H. DeStaebler, "Photon-Induced Residual Activity," Rept. No. SLAC-TN-63-92, Stanford Linear Accelerator Center, Stanford University, Stanford, California (1963).
- 55 R. J. Debs, J. T. Eisinger, A. W. Fairhall, I. Halpern, and H. G. Richter, *Phys. Rev.* **97**, 1325 (1955).

- 56 H. DeStaebler, "Tritium Production in Water," Rept. No. SLAC-TN-64-6, Stanford Linear Accelerator Center, Stanford University, Stanford, California (1964).
- 57 D. Coward, private communication, Stanford Linear Accelerator Center, Stanford University, Stanford, California.
- 58 H. DeStaebler, "Electron-Photon Flux in the Tunnel When the Machine is on: Applications to Chemically Active Air and to Active Cooling Water," Rept. No. SLAC-TN-62-76, Stanford Linear Accelerator Center, Stanford University, Stanford, California (1962).
- 59 H. DeStaebler, Jr., "Radioactive Gas in the Tunnel," Rept. No. SLAC-TN-62-9, Stanford Linear Accelerator Center, Stanford University, Stanford, California (1962).
- 60 B. P. Nigam, M. K. Sundaresan, and Ta-You Wu, *Phys. Rev.* **115**, 491 (1959).

